Acta Cryst. (1998). A**54**, 83-90

The Influence of Phonon Scattering on HREM Images

G. Möbus,* T. Gemming and P. Gumbsch

Max-Planck-Institut für Metallforschung, Seestrasse 92, D-70174 Stuttgart, Germany.
E-mail: moebus@hrem.mpi-stuttgart.mpg.de

(Received 1 April 1997; accepted 5 September 1997)

Abstract

The influence of thermal atomic vibrations in high-resolution electron microscopy is modeled by combining time-resolved molecular dynamics simulations with the multislice algorithm of HREM image simulation. The material studied is stoichiometric NiAl-*B*2 at room temperature and at 900 K. The difference between the new method of image calculation and conventional calculations by Debye–Waller factors and absorption parameters is examined in detail. The difference between images calculated with and without thermal diffuse scattering (TDS) is found to be surprisingly small owing to the small thickness of typical HREM specimens of about 10 nm.

1. Introduction

The simulation of high-resolution transmission electron microscopy (HREM) images usually accounts for temperature effects by the implementation of Debye–Waller factors (DWF). The recent development of HREM towards *in situ* experiments where lattice fringe images are recorded at temperatures of up to 1000 K makes it necessary to study the influence of temperature more precisely. A check of the precision of the DWF approximation is especially important since the required accuracy of HREM simulations increases by the upcoming of digital image matching between simulated and experimental images. Since each approximation involved in the image-simulation software might lead to a systematic error in the retrieved structure model, there is an increasing interest in judging the order of magnitude of this error. Some approximations might result in negligible structural errors but others may not.

The influence of temperature on electron diffraction consists first of an attenuation of the intensity of the Bragg spots, which represent the coherent elastic wave field of electrons scattered by a perfect crystal. At the same time, the reciprocal space between the spots is filled with thermal-diffuse-scattering intensity (TDS). This effect is modeled in diffraction simulation programs by two parameter sets (see *e.g.* Cowley, 1981), schematically illustrated in Fig. 1: (i) element-dependent Debye–Waller factors (DWF) reduce the scattering power of the atoms due to thermal vibrations and lead to a weakening of high-order diffracted spots relative to the zero beam (as if intensity would be scattered back to the undiffracted beam); (ii) an imaginary part of the complex scattering potential, dependent on element and scattering angle and to be multiplied by the Debye–Waller factor, accounts for the loss of inelastically scattered electrons from the elastic wavefield. This absorption weakens both the diffracted ('anomalous absorption') and the undiffracted beams and is meant to substitute the diffuse background contribution (Fig. 1).

2. Definition of the problem

In order to check the influence of elevated temperature on HREM images, we selected as a specific test material the intermetallic alloy NiAl which crystallizes in the *B*2 structure. Apart from the actual interest in NiAl from a materials science point of view, the choice was motivated by the availability of a reliable interatomic potential, necessary in order to do atomistic simulations of the crystal structure (Ludwig & Gumbsch, 1995).

Image simulations for high temperatures including phonon scattering require the knowledge of the crystal structure variations over a certain period of time. We follow the frozen lattice model as described by Wang

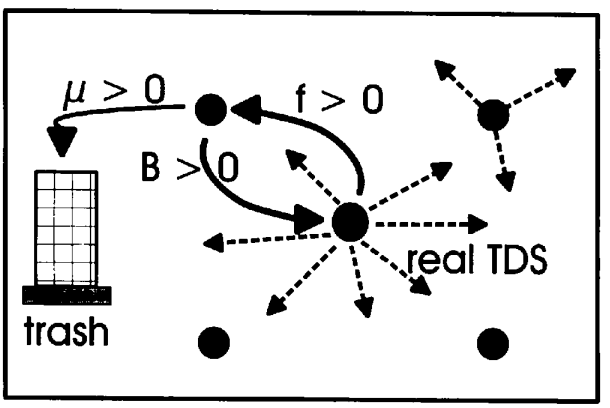

Fig. 1. Illustration of the relative diffraction intensity changes when temperature is increased from $T = 0$. Real world thermal diffuse scattering (TDS) and the simulation with Debye–Waller factor (exponent B), atomic form factor f and absorption index μ are compared.

(1995) as a semiclassical theory for thermal diffuse scattering with many beams. This approach neglects the energy loss of the electrons and is based on a high-energy approximation for the fast electrons, which see the vibrating crystal at rest.

During a finite exposure time τ, the image intensity is given by the time integral:

$$I(k) = \int_0^\tau I(k, t)\,\mathrm{d}t \tag{1}$$

with k denoting the spatial frequency and t the time. This means that the averaging is performed not earlier than in the image plane while, on the other hand, Debye–Waller-factor (DWF) theory uses averaging in the 'crystal plane'. The integrand $I(k, t)$ is to be calculated dynamically from a single slice scattering potential $S(k, t)$, *e.g.* using the conventional multislice procedure, but without any absorption and DWFs. For a two-atom structure consisting of Ni and Al (described in detail in §3), we have:

$$\begin{aligned} S(k, t_i) &= \int U(r, t_i)\exp(-ikr)\,\mathrm{d}V \\ &= \sum_{j,\mathrm{Ni}} \int U_{\mathrm{Ni}}(r, t_0)\exp\{-ik[r - r_j(t_i)]\}\,\mathrm{d}V \\ &\quad + \sum_{j,\mathrm{Al}} \int U_{\mathrm{Al}}(r, t_0)\exp\{-ik[r - r_j(t_i)]\}\,\mathrm{d}V \\ &= \sum_{j,\mathrm{Ni}} f_{\mathrm{Ni}}(k)\exp[-ikr_j(t_i)]\,\mathrm{d}V \\ &\quad + \sum_{j,\mathrm{Al}} f_{\mathrm{Al}}(k)\exp[-ikr_j(t_i)]\,\mathrm{d}V. \end{aligned} \tag{2}$$

Here U stands for the crystal scattering potential distribution, $U(t_0)$ for the scattering potential of a single atom j (Ni or Al) at a fixed (but arbitrary) time t_0 and f for the atomic scattering factor for electrons.

After an average over many vibrational crystal structures (*e.g.* in the Einstein, Debye or other non-correlated vibrational approximation), the conventional scattering formula (as implemented in HREM-simulation packages) results as:

$$\begin{aligned} S(k) &= \langle S(k, t)\rangle \\ &= \sum_{j[\mathrm{Ni}]} \exp(-ik\langle r_j\rangle)[f_{\mathrm{Ni}}(k) + if'_{\mathrm{Ni}}(k)]\exp[-B_{\mathrm{Ni}}k^2] \\ &\quad + \sum_{j[\mathrm{Al}]} \exp(-ik\langle r_j\rangle)[f_{\mathrm{Al}}(k) + if'_{\mathrm{Al}}(k)]\exp[-B_{\mathrm{Al}}k^2]. \end{aligned} \tag{3}$$

Here the Debye–Waller factor with exponent B reveals a true time average, while the absorptive form factor f', which is an imaginary part added to the elastic form factor f, indirectly accounts for the intensity loss that occurs if the diffuse averaged intensity is no longer considered in the simulations. Equation (3) simplifies the more realistic formula (2) with respect to the following four effects:

(i) The Einstein model commonly involved in Debye–Waller factors assumes independent vibrations of neighboring atoms, thus neglecting the actual phonon spectrum.

(ii) The vibration potential is assumed to be harmonic.

(iii) The potential and the DWF are fixed to be isotropic (at least for common HREM-simulation packages).

(iv) The diffuse spectrum (TDS) is removed from the calculations by the absorptive form factor while in reality it is propagated to the image by the objective lens in just the same way as the elastic periodic scattering.

Attempts to improve simulation software beyond the most simple approach of single Debye–Waller factors and single numbers for the absorption (ratio between imaginary and real parts of the scattering potential) are numerous: Kohl & Rose (1985), Wang (1989), Cowley (1989), and Fanidis *et al.* (1992) describe the theory of inelastic scattering due to thermal or other scattering sources (see also citations therein). Bird & King (1990) as well as Weickenmeier & Kohl (1991) deduce a data base for element- and frequency-dependent absorptive factors for simulation programs.

Detailed calculations of thermal diffuse scattering for HREM have not been performed for a long time. In fact, the phonon contributions might be expected to be incoherent and therefore negligible. The contribution of phonons to real-space images is certainly much smaller than to diffraction patterns, since the randomness of the phases leads to a cancellation of the individual phonon images (time and spatial averaging).

Recent publications, however, examined a possible influence of TDS on HREM images: First, considerations of the scattering intensity distribution for phonon-scattered electrons lead to the prediction by Cowley (1988, 1989) that HREM images, exclusively formed by phonon-scattered electrons, might show sharper details (higher resolution) compared to the elastic image. Another approach by Rez (1993) extended this study to a calculation of many-beam HREM images (line profiles) for a single phonon frequency as well as for an average of phonon frequencies for different phonon dispersion relations. The result was that the phonon contribution is on the order of $<1\%$ of the image contrast, but even more attenuated (and unobservable) for a dispersion average. Another approach by Dinges & Rose (1995) and Dinges, Berger & Rose (1995) uses a multislice algorithm with a phase-randomizing technique, which allows inclusion of TDS scattering as if it was coherent in a first step. With the use of the Einstein approximation, they calculated phonon images and diffraction patterns for various types of microscopy. For the case of STEM and also based on the Einstein approximation of thermal vibrations, frozen phonon calculations are presented by Hillyard & Silcox (1993).

Here an attempt will be made to include a complete and realistic phonon spectrum in HREM-image simula-

tions and to check if the recently predicted TDS contributions to HREM images are significant or marginal.

3. The molecular dynamics approach

Atomistic simulations by molecular dynamics lead to crystal structures that comprise the average (static) equilibrium structure C_0 as well as the time-resolved modifications of this structure $C_i(t_i)$ owing to thermal vibrations. From a large number of structures $C(t_i)$, the statistical fluctuations of the crystal can be drawn in real space. From a statistical analysis of the real-space data, it is possible to obtain (i) the frequency-resolved phonon spectrum of the crystal (Gumbsch & Finnis, 1996), as well as (ii) Debye–Waller factors with element-dependent and, in principle, anisotropic values. In the present work, however, the real-space data are only used to directly derive many thin slices ($m = 1$ to 24) with a thickness of a monolayer. These slices are used as periodic supercells for the multislice method of HREM-image simulations and contain the atomic displacements during thermal movement at a specific time. Equation (2) then reads

$$S_m(k, t_i) = \sum_{j,\mathrm{Ni}} f_{\mathrm{Ni}}(k) \exp[-ik\langle r_j\rangle + u_{jm}(t_i)]\,\mathrm{d}V + \sum_{j,\mathrm{Al}} f_{\mathrm{Al}}(k) \exp[-ik\langle r_j\rangle + u_{jm}(t_i)]\,\mathrm{d}V \quad (4)$$

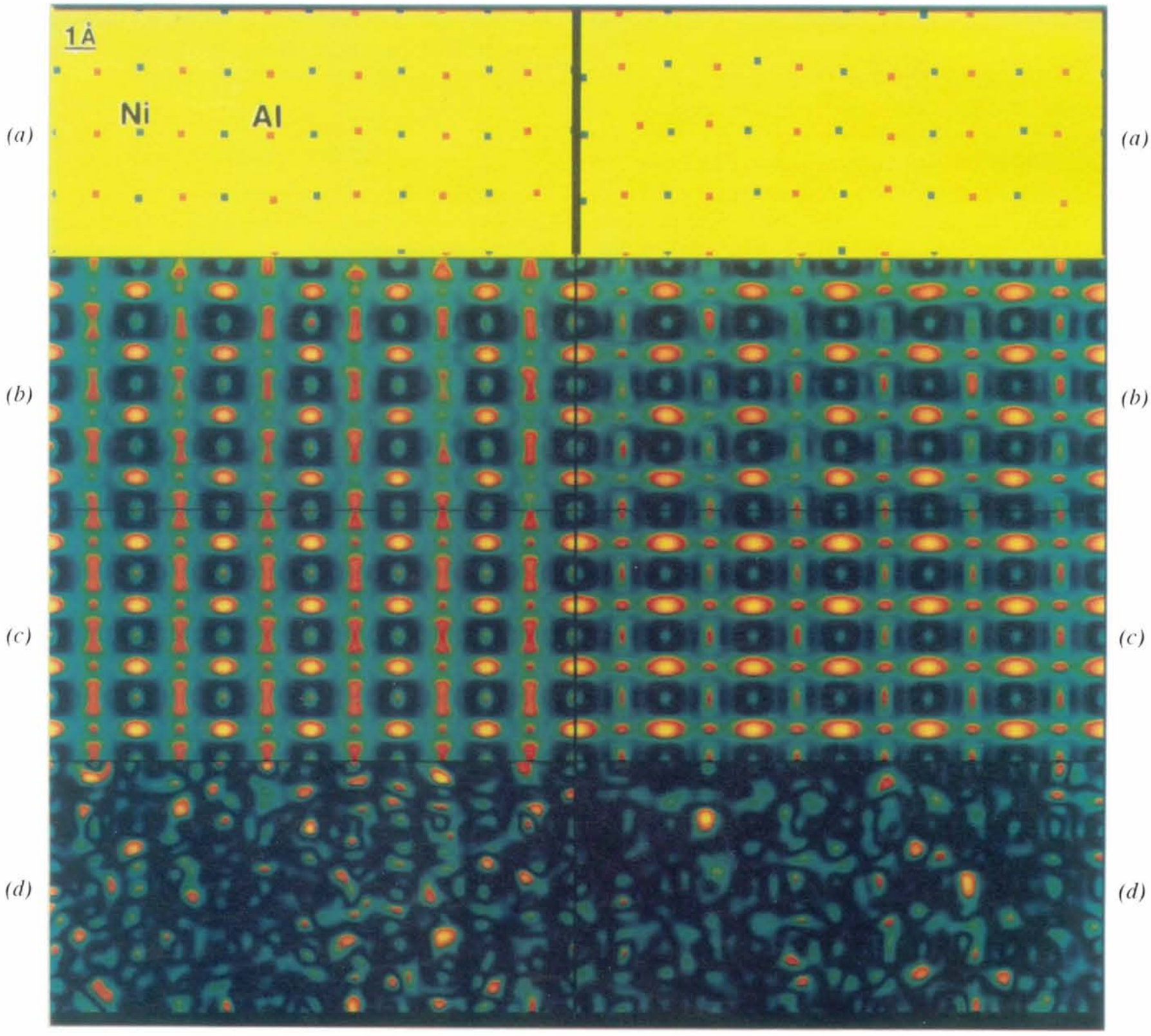

Fig. 2. (i) (*a*) Small section of a molecular-dynamics-generated single-slice supercell of NiAl ⟨110⟩ as used for the multislice calculations. Valid for a temperature of 300 K. (*b*) Single time image calculated for a thickness of 24 slices of NiAl and the Scherzer focus imaging condition of the microscope JEM ARM1250 Stuttgart at 1250 kV. (*c*) Incoherent addition of snapshot images of the kind of (*b*). (*d*) Difference image between (*b*) and (*c*), enhanced by a factor of 10 to make the small fluctuations visible. (ii) Same as (i) but for 900 K.

with u the displacement of atom j of slice m and t_i the time of the snapshot.

For our molecular-dynamics-assisted HREM simulations, it is especially important to select a material with a reliable interatomic potential, which is the case for NiAl (Ludwig & Gumbsch, 1995). The vibrational properties of this potential are proven to be realistic by calculations of the phonon spectrum (Gumbsch & Finnis, 1996). Another important check of the reliability of the potential is the comparison of DWFs derived from the phonon spectrum to experimental DWF values. Experimental measurements can be obtained for Ni and Al using quantitative convergent-beam electron diffraction (CBED) calculations (Nüchter *et al.*, 1995), as well as using refinements of X-ray diffraction patterns (Georgopoulos & Cohen, 1977). The agreement between theory and experiment was shown to be excellent (Gumbsch & Finnis, 1996).

The selected geometry has to account for typical experimental HREM conditions (specimen thickness as small as 10 nm) as well as for the need of the molecular dynamics method to avoid finite cell effects by restricting the phonon frequency spectrum. A rectangular volume of $4.9 \times 5.1 \times 10$ nm with the three axes aligned along $\langle 001 \rangle \times \langle 1\bar{1}0 \rangle \times \langle 110 \rangle$ directions of NiAl and a free surface perpendicular to the z axis was found to give a reasonable compromise between computational effort and realistic specimen dimensions. This sample was first equilibrated in the computer for 800 ps at a temperature of 300 K by rescaling velocities to guarantee a constant kinetic energy. After this equilibration period, 100 snapshots were taken at random times during the following 500 ps.

For the 900 K simulation, we started from the equilibrated 300 K structure and scaled the velocities up to a kinetic energy corresponding to 900 K. After equilibration for another 250 ps, we took another 20 snapshots during the following 100 ps. Standard molecular-dynamics (MD) techniques with a centered difference integration scheme and a time step of $\Delta t = 2$ fs are used (Allen & Tildesley, 1987).

For the image simulations, the long axis of the rectangular NiAl volume was chosen to be parallel to the incident-beam direction. A thickness of two (220) planes per slice was selected for the multislice algorithm, leading to 24 slices, each consisting of 1325 atoms, sampled in 1024×1024 pixels. A single-time real-space image $I_i(x, y; t_i)$ then results from the dynamical multislice calculations and the subsequent nonlinear image calculation (see details in §4).

To account for the long experimental exposure times, many images at different t_i have to be calculated and to be added incoherently.

$$I(x, y) = (1/N) \sum_{i}^{N} I_i(x, y; t_i). \qquad (5)$$

The minimum number of snapshots N has been established empirically by the condition that there is no change visible in the image intensity when adding a further image. For real-space image analysis, 20 images are enough. More sensitive to changes in the diffuse spectrum are diffractograms $D(k_x, k_y) = |\mathrm{FFT}[I(x, y)]|$. Here up to 70 snapshots have been added.

With the approach described above, three of the four items mentioned in the *Introduction* to describe realistic thermal diffuse scattering are included, namely correlated vibrations (phonons), anharmonic vibrations and imaging of the diffuse spectrum. A possible anisotropy of the vibrations corresponding to anisotropic Debye–Waller factors does not come into play because of the cubic symmetry of the selected material. The wavelength change of electrons inelastically scattered by phonons is considered to be negligible. We attempt to benefit from the MD calculations with respect to predictions of possible fine details in diffractograms, which are not included in an Einstein model of vibrations.

4. Multislice calculations

The image simulation software *EMS* (Stadelmann, 1987) has been selected for the processing of the supercells. Fig. 2(i) presents the different stages of image simulation using the atom coordinates calculated from room-temperature MD calculations (300 K). Fig. 2(ii) presents the equivalent data for the high-temperature (900 K). Only a small area (about 1/100) of the actually processed supercells is displayed in Fig. 2. The input data into *EMS* are atom coordinates fluctuating around their equilibrium positions [Fig. 2(i)(*a*)]. The *EMS* program *pa3* (Stadelmann, 1987) is used to calculate the exit wave function. Finally, *EMS im1* leads to a single time image [Fig. 2(i)(*b*)]. No DWF or absorption is used for this calculation. The slight lateral fluctuations in Fig. 2(i)(*b*) vanish apparently after the incoherent addition of intensities for many snapshots [Fig. 2(i)(*c*)]. The difference image between Figs. 2(i)(*b*) and (*c*) highlights the fluctuations [Fig. 2(i)(*d*)]. Throughout this work, all imaging data are selected to match the JEM ARM1250 Stuttgart microscope, with $C_s = 1.6$ mm, underfocus of 34 nm, 1250 kV, focus spread of 10 nm and beam convergence of 0.3 mrad.

On a fast workstation (DEC-Alpha-8400) equipped with >1 Gbyte memory, it took 6 h to calculate a single time image by *EMS* and a few weeks for the time-integrated image.

Figs. 2(ii)(*a*)–(*d*) show the corresponding high-temperature calculations at 900 K with an increase in the vibration amplitude of the atoms most easily seen by comparing Fig. 2(ii)(*a*) to Fig. 2(i)(*a*).

The contribution of the diffuse phonon spectrum can best be recognized in the diffractograms $D = |\mathrm{FFT}[I(x, y)]|$. For a single time t_i, the diffuse spectrum shows a streaky structure. In Fig. 3(*a*), the Bragg spot intensities had to be cut in order to make the background

visible. For the time-average image (Fig. 3*b*), the diffuse part of the diffractogram has just weakened without much change of the details. For better visibility, the Bragg spots in Fig. 3(*b*) are therefore cut at a threshold 10 times lower than in Fig. 3(*a*). Two distinct streaky features between the Bragg spots of the averaged spectrum can be observed: dark bands in the middle between Bragg spots (double arrow on Fig. 3*b*) and weak satellite reflections or small bright bands in the vicinity of Bragg spots (single arrow on Fig. 3*b*). The existence of these features is basically independent of the number of HREM images added. However, the intensity of both streaks and satellite peaks relative to their neighboring Bragg spots drops with the number of image additions. This intensity drop of all background features is to be discussed later by comparison to observations on diffraction patterns instead of diffractograms. The orientation of streaks, dark bands and satellite spots is well correlated to **k** vectors (differences between strong Bragg spots) observed equivalently for several neighboring Bragg spots.

Because the Bragg spots are cut, it is no longer visible that the background features are stronger for strong Bragg spots as compared to weak spots. On the other hand, there is no correlation to the edges of the chosen supercell. This indicates that we are neither observing an artefact of the MD supercell nor just a noisy feature.

For thick crystals (>100 nm), experimental observations of streaks from thermal diffuse scattering are observed in the diffraction pattern. Examples of simple metals and semiconductors are found in Wang (1995). For the case of NiAl, there is a formal relationship of these features to the phenomenon of spectra from tweed structures observed in experimental diffraction patterns from nonstoichiometric NiAl (Zheng & Stobbs, 1995). The phenomenon of 'tweeding' is supposed to be caused by static displacement waves induced by relaxations around point defects (vacancies and substitutional elements), which are needed to realize the deviation from stoichiometry. Our results, on the other hand, are calculated for stoichiometric NiAl without static displacement waves. There is an important difference between static displacement waves and phonons. While the diffraction patterns observed in the two cases might look similar (independent of the observation time), the diffuse contribution of phonons to the image or diffractogram (*i.e.* the FFT of the image) tends to cancel after averaging over the phonon spectrum for an integration time large enough to avoid accidental features.

As has been pointed out in §2, the random phases of the phonon contributions lead to an apparent incoherence. However, we have to be aware that the weakening of the diffuse image contribution observed here might converge asymptotically against a very weak but nonzero background. We conclude that the existence of any phonon-related image detail in HREM images from 10 nm thick NiAl, which would survive the integration procedure after infinite addition of images, cannot be proven but must at least be weaker than 0.1% of the elastic image contrast. Unlike diffraction patterns, there is no evidence that any phonon-related peaks or streaks could be found in a diffractogram from an experimental HREM image.

To study the influence of temperature, a comparison of the two spectra for each temperature (300 and 900 K) is presented as Figs. 3(*c*), (*d*). The spot-to-background ratio decreases by a factor of three towards the higher temperature. The streaky appearance remains qualitatively unchanged.

5. Comparison to DWF-based image simulations

Before judging the amount of difference between the molecular-dynamics-based HREM simulation ('MD image') and the DWF-based image, it is necessary to make sure that the conventional simulations are optimized to result in the most similar image to the MD image. For this purpose, a multidimensional fit is performed. In this fit, the MD image plays the role of the experimental image otherwise used in iterative digital image matching in quantitative HREM [Möbus & Rühle (1994), Möbus & Dehm (1996)]. As an image agreement measure, the following R factor has been selected:

$$R = \left[\sum (E_{ij} - S_{ij})^2\right] \Big/ \left[\sum (E_{ij})^2\right] \qquad (6)$$

with E denoting the MD image and S the conventional simulation. The configuration space for optimization is found to be four-dimensional (at maximum) because of the fixed specimen thickness and imaging parameters (focus, resolution). Variables are first of all the two Debye–Waller factors for Ni and Al. In case there is no analytical absorption program available, there is an absorption index ($\mu = f_i/f_r$) to be considered as the third variable. Since none of these three variables considers the correlated vibration of atoms forming the MD image, one could try to include a vibrational envelope [modulation transfer function (MTF) with Gaussian half-width ρ, $\mathrm{mtf}(k) = \exp(-\pi^2\rho^2k^2)$] as a fourth variable to account at least for the combined vibration corresponding to a phonon with infinite wavelength. Such a vibrational envelope is part of many image-simulation packages meant to simulate mechanical vibrations, drift of specimen or the limited resolution of the recording medium. The optimization vector is therefore defined by $\{B(\mathrm{Ni}), B(\mathrm{Al}), \mu, \rho\}$.

The comparison is presented for a small section of two unit cells only. Fig. 4(*a*) shows the zero-vibration image and Fig. 4(*b*) the projected potential to illustrate the corresponding supercell. The MD images [Fig. 4(*c*) for 300 K and Fig. 4(*d*) for 900 K] are the time-averaged images [Fig. 2(i)(*c*) and Fig. 2(ii)(*c*), respectively], and contain two unit cells of the final result of the molecular-

dynamics approach at both temperatures. Fig. 4(*e*) is the fitted conventional room-temperature calculation and Fig. 4(*f*) the high-temperature fit. The difference images between the conventional and MD calculations are given at the bottom.

The route to the best fit applied here can be described as a pair-wise search:

(i) vary only the two DWFs for Ni and Al while absorption is kept constant (taken from the program *atom.f* by Bird & King (1990) resulting in an R factor of $R = 0.64\%$ (300 K) and $R = 0.47\%$ (900 K).

(ii) Consider μ (absorption) and ρ (MTF constant) as a pair of variables (without using *atom.f*): if one starts from the best fitting DWF values of (i), the R factor changes to $R = 0.66\%$ (300K) and $R = 0.54\%$ (900 K).

Since especially $\mu = 0$ gives a suboptimal result, the usefulness of including absorption parameters in the HREM calculations at all is verified. The inclusion of a MTF to approximate long-range phononic correlations must, however, be rejected because the best fit for all absorption values is obtained for $\rho = 0$. It is noted that the procedure of multiparameter fitting is meant to lead to the most similar image compared to the MD image, not to the most similar DWFs when compared directly to the mean vibration amplitudes $\langle u^2 \rangle$ of the MD-input data. Nevertheless, the fitted DWF exponents of $B(\mathrm{Ni}) = 0.005$ and $B(\mathrm{Al}) = 0.004\ \mathrm{nm}^2$ for 300 K are consistent within the fitting precision with the B values directly calculated from the mean vibrational amplitudes: $B = 0.0046\ \mathrm{nm}^2$ and $\langle u \rangle = 0.076$ nm for Ni and $B = 0.0040\ \mathrm{nm}^2$ and $\langle u \rangle = 0.071$ nm for Al (Gumbsch & Finnis, 1996).

When comparing the two results for different temperatures, it is interesting to note that the deviation of the

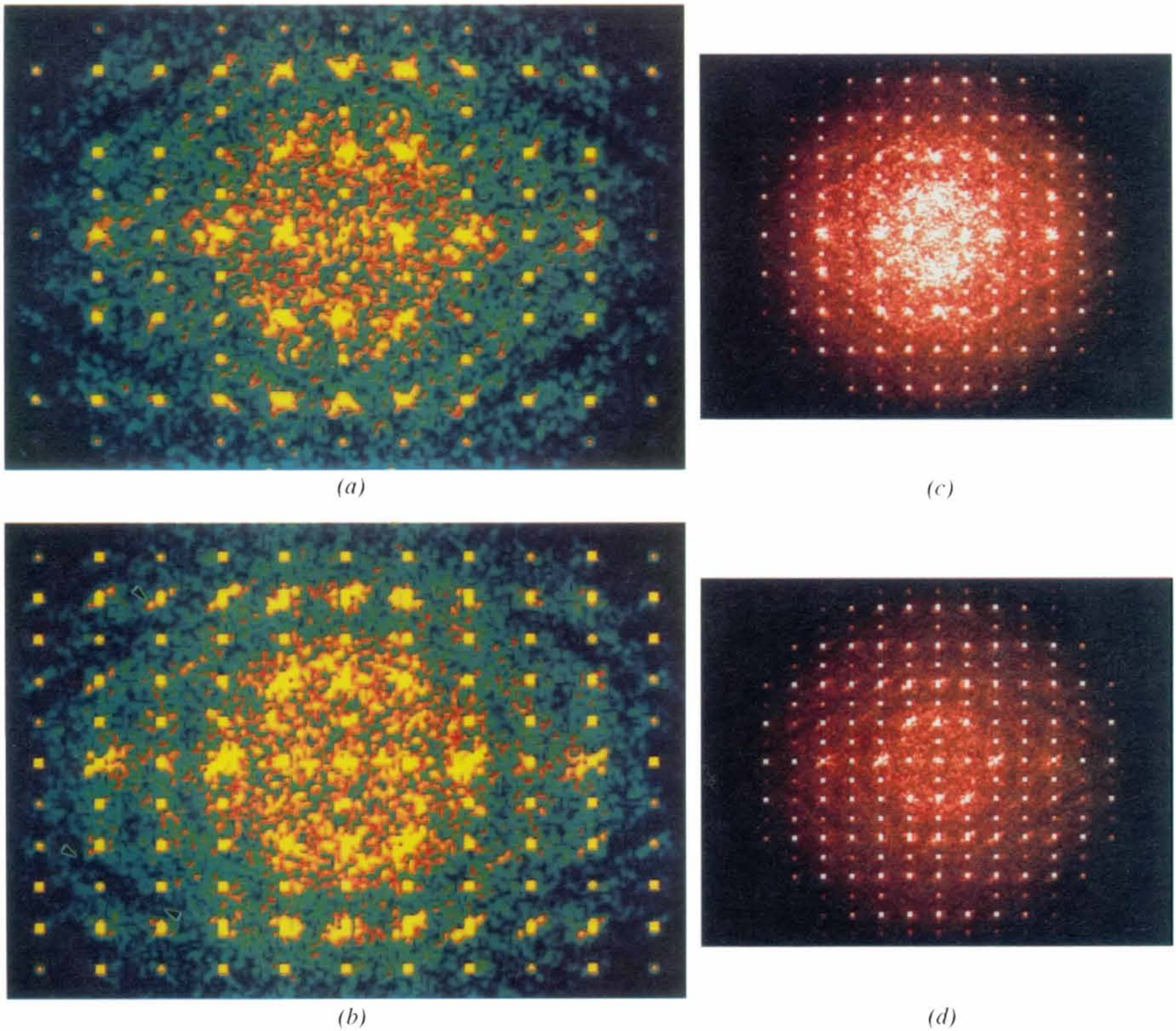

Fig. 3. Diffractograms of images calculated by the molecular dynamics and multislice procedures. (*a*) Single time image for room temperature, (*b*) incoherent addition for room temperature. The background is enhanced compared to (*a*) by a factor of 8. (*c*) Full size diffractogram at 900 K. (*d*) Full size diffractogram at 300 K.

best fitting conventional image from the corresponding MD image at the same temperature is even smaller for the higher temperature.

6. Discussion and summary

The presented method of calculating high-temperature images relies on the availability of a simple, yet reliable, atomic interaction model and is still highly computing intensive and can therefore not be considered to become a standard method. The importance of the method lies in providing highly accurate reference data including (multiple-) thermal diffuse scattering with a realistic correlated phonon spectrum. These data are to be used for checking faster procedures of calculations accounting for thermal diffuse scattering or high temperatures.

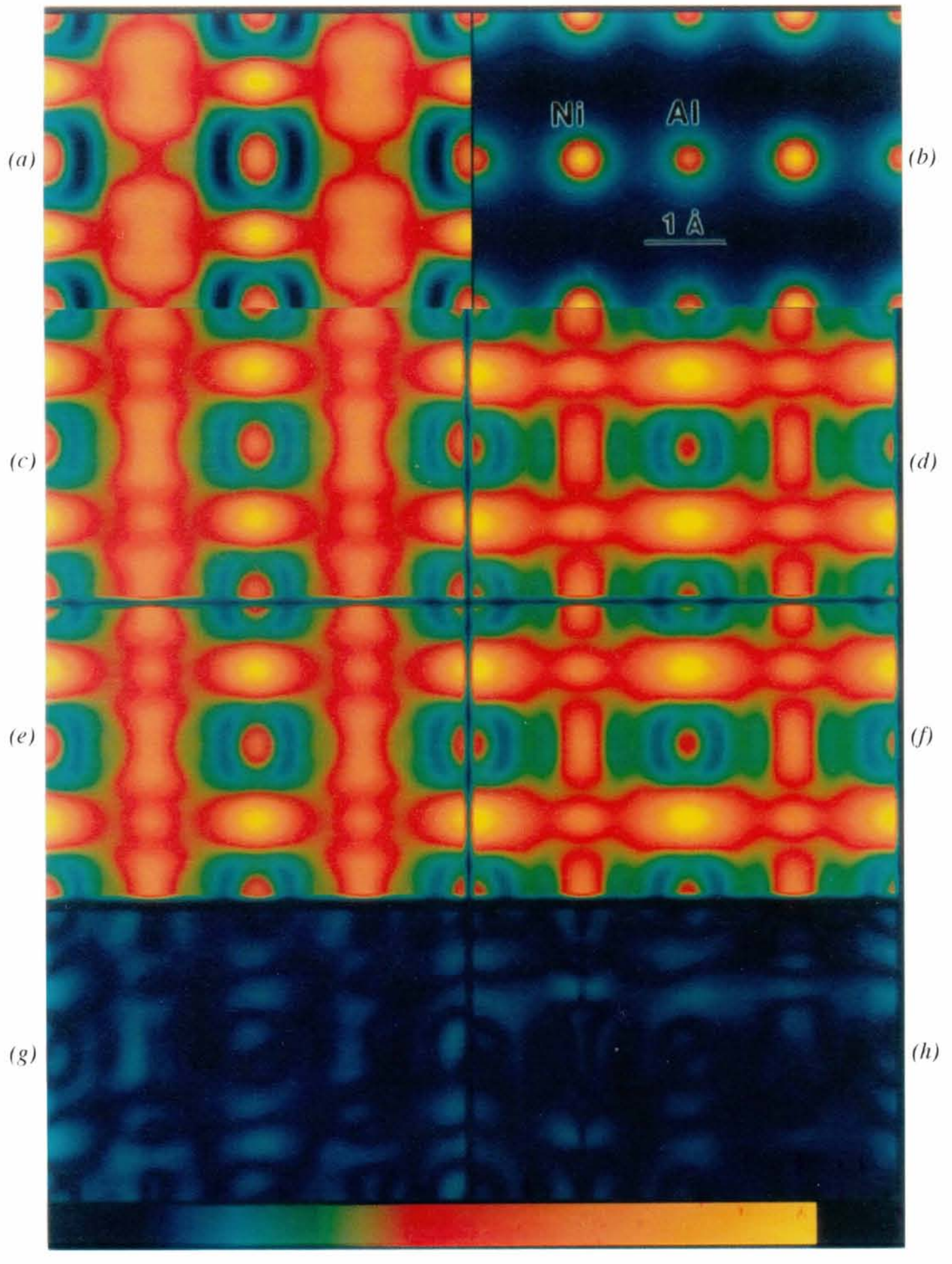

Fig. 4. Two unit cells of NiAl ⟨110⟩. (*a*) Zero-temperature conventional simulation, (*b*) single-slice transmission function (imaginary part) to illustrate the geometry. (*c*), (*d*) Molecular-dynamics-simulated time-averaged images for 300 K (left) and 900 K (right). (*e*), (*f*) Best fitting conventional simulations for 300 K (left) and 900 K (right). (*g*), (*h*) Difference images of the two kinds of image simulations above.

Mainly, the usefulness of combining Debye–Waller factors with absorptive factors could be proven so that the implementation of absorption programs (Bird & King, 1990; Weickenmeier & Kohl, 1991) into image simulations can be recommended also for HREM of thin specimens although it does not appear to be crucial. A comparison of the MD results to the program of Dinges & Rose (1995) is planned for the future.

The surprisingly small difference between the molecular-dynamics-based HREM image and the Debye–Waller-factor-based image shows primarily that thermal diffuse scattering must be considered to be negligible for real-space images from HREM specimens of 10 nm thickness and below for NiAl. The molecular-dynamics approach does not allow calculation of an exclusive phonon image, but only the combination of the zero-vibration image and the phonon images. Thus, earlier predictions on spot sharpening by phonons (Cowley, 1989; Rez, 1993) cannot be checked. Since there is no distinct feature visible in real space related to the correlated vibrations of atoms, the Einstein approximation of independent atomic vibrations must also be considered as of high quality. The improvement of accuracy expected from the MD calculations could not be proven experimentally since the difference between an experimental image and any kind of simulation far exceeds the difference between the two methods of image simulation. This also means that thermal diffuse scattering does not have an influence on the atomic coordinates obtained by structure retrieval *via* quantitative HREM [iterative digital image matching (Möbus & Rühle, 1994)]. It is to be noted, however, that the influence of anisotropic vibrations could not be demonstrated here since the selected material was cubic.

Discussing the problem in reciprocal space leads to slightly different conclusions. Looking at the diffractograms (*i.e.* the Fourier transform of the high-resolution image), we found a distinct background contribution between Bragg spots owing to the diffuse scattering which is exclusive to the MD simulations because it is compared against a zero background in the conventional simulations. There is also a clear fingerprint due to the correlated vibrations visible in the form of a streaky spectrum between the Bragg spots. The background from an Einstein model of vibrations would be featureless. However, the experimental verification of these features fails just as well, because of other experimental contributions to the diffuse spectrum being much stronger. Mainly amorphous layers at the surfaces of the sample must be considered here, but also point defects in the material, unavoidable noise from the recording medium and shot noise. This negative expectation must again be distinguished from diffraction patterns, recorded in the microscope. Because of the missing attenuation by the superposition of random phonon phases, an observation of the diffuse background as well as the distinct streaking is much easier, and has in fact been demonstrated (see Wang, 1995 for examples).

Finally, it is mentioned that the importance of thermal diffuse scattering increases towards lower acceleration voltages than the calculated 1250 kV, as well as towards higher specimen thicknesses than the calculated 10 nm [especially for CBED, CTEM and STEM/Z contrast (Pennycook & Jesson, 1991)], as has been shown by several authors (Hillyard & Silcox, 1993; Dinges & Rose, 1995).

We thank Mike Finnis for motivating this work and Christoph Dinges and Andreas Weickenmeier for helpful advice.

References

Allen, M. P. & Tildesley, D. J. (1987). *Computer Simulation of Liquids*. Oxford Science Publications.
Bird, D. M. & King, Q. A. (1990). *Acta Cryst.* A**46**, 202–208.
Cowley, J. M. (1981). *Diffraction Physics*, 2nd ed. Amsterdam: North-Holland.
Cowley, J. M. (1988). *Acta Cryst.* A**44**, 847–853.
Cowley, J. M. (1989). *Computer Simulation of Electron Microscope Diffraction and Images*, edited by W. Krakow & M. O'Keefe, pp. 1–12. Warrendale, PA: TMS.
Dinges, C., Berger, A. & Rose, H. (1995). *Ultramicroscopy*, **60**, 49–71.
Dinges, C. & Rose, H. (1995). *Phys. Status Solidi A*, **150**, 23–30.
Fanidis, C., Van Dyck, D. & Van Landuyt, J. (1992). *Ultramicroscopy*, **41**, 55–64.
Georgopoulos, P. & Cohen, J. B. (1977). *Scr. Metall.* **11**, 147–150.
Gumbsch, P. & Finnis, M. (1996). *Philos. Mag. Lett.* **73**, 137–144.
Hillyard, S. & Silcox, J. (1993). *Ultramicroscopy*, **52**, 325–334.
Kohl, H. & Rose, H. (1985). *Adv. Electron. Electron Phys.* **65**, 173–227.
Ludwig, M. & Gumbsch, P. (1995). *Modelling Simul. Mater. Sci. Eng.* **3**, 533–542.
Möbus, G. & Dehm, G. (1996). *Ultramicroscopy*, **65**, 217–228.
Möbus, G. & Rühle, M. (1994). *Ultramicroscopy*, **56**, 54–70.
Nüchter, W., Weickenmeier, A. & Mayer, J. (1995). *Inst. Phys. Conf. Ser.* No. 147, 129–132.
Pennycook, S. J. & Jesson, D. E. (1991). *Ultramicroscopy*, **37**, 14–38.
Rez, P. (1993). *Ultramicroscopy*, **52**, 260–266.
Stadelmann, P. (1987). *Ultramicroscopy*, **21**, 131–146.
Wang, Z. L. (1989). *Acta Cryst.* A**45**, 193–199.
Wang, Z. L. (1995). *Elastic and Inelastic Scattering in Electron Diffraction and Imaging*. New York: Plenum Press.
Weickenmeier, A. & Kohl, H. (1991). *Acta Cryst.* A**47**, 590–597.
Zheng, Y. & Stobbs, W. M. (1995). *Inst. Phys. Conf. Ser.* No. 147, 353–356.